Monthly Notices of the ROYAL ASTRONOMICAL SOCIETY

MNRAS **529,** 1827–1838 (2024) https://doi.org/10.1093/mnras/stae647
Advance Access publication 2024 March 4

Imposters among us: globular cluster kinematics and the halo mass of ultra-diffuse galaxies in clusters

Jessica E. Doppel [1,2,3★] Laura V. Sales [1] José A. Benavides [1] Elisa Toloba [4] Eric W. Peng [5] Dylan Nelson [6] and Julio F. Navarro [7]

[1]*Department of Physics and Astronomy, University of California, Riverside, 900 University Ave, Riverside, CA 92521, USA*
[2] *Institute for Computational Cosmology, Department of Physics, Durham University, South Road, Durham DH1 3LE, UK*
[3]*Centre for Extragalactic Astronomy, Department of Physics, Durham University, South Road, Durham DH1 3LE, UK*
[4]*Department of Physics, University of the Pacific, 3601 Pacific Avenue, Stockton, CA 95211, USA*
[5]*NSF's National Optical-Infrared Astronomy Research Laboratory, 950 North Cherry Avenue, Tucson, AZ 85719, USA*
[6]*Universität Heidelberg, Zentrum für Astronomie, Institut für Theoretische Astrophysik, Albert-Ueberle-Str. 2, 69120 Heidelberg, Germany*
[7]*Department of Physics and Astronomy, University of Victoria, Victoria, BC V8P 5C2, Canada*

Accepted 2024 March 1. Received 2024 March 1; in original form 2023 September 6

ABSTRACT

The velocity dispersion of globular clusters (GCs) around ultra-diffuse galaxies (UDGs) in the Virgo cluster spans a wide range, including cases where GC kinematics suggest haloes as massive as (or even more massive than) that of the Milky Way around these faint dwarfs. We analyse the catalogues of GCs derived in post-processing from the TNG50 cosmological simulation to study the GC system kinematics and abundance of simulated UDGs in galaxy groups and clusters. UDGs in this simulation reside exclusively in dwarf-mass haloes with $M_{200} \lesssim 10^{11.2}$ M$_\odot$. When considering only GCs gravitationally bound to simulated UDGs, we find GCs properties that overlap well with several observational measurements for UDGs. In particular, no bias towards overly massive haloes is inferred from the study of bound GCs, confirming that GCs are good tracers of UDG halo mass. However, we find that contamination by intracluster GCs may, in some cases, substantially increase velocity dispersion estimates when performing projected mock observations of our sample. We caution that targets with less than 10 GC tracers are particularly prone to severe uncertainties. Measuring the stellar kinematics of the host galaxy should help confirm the unusually massive haloes suggested by GC kinematics around some UDGs.

Key words: galaxies: dwarf – galaxies: haloes – galaxies: clusters: intracluster medium – galaxies: star clusters: general.

1 INTRODUCTION

Ultra-diffuse galaxies (UDGs), galaxies of extremely low-surface brightness for their stellar mass, are enigmatic systems whose origin remains unclear. While the presence of such objects has been known for several decades (see e.g. Reaves 1983; Binggeli, Sandage & Tammann 1985; Impey, Bothun & Malin 1988; Bothun, Impey & Malin 1991; Dalcanton et al. 1997), a renewed interest in these systems has been sparked by a series of studies of UDGs in the Coma Cluster (see Abraham & van Dokkum 2014; van Dokkum et al. 2015a, b). UDGs were thought to reside primarily in the environments of galaxy groups or clusters (see van Dokkum et al. 2015b; Koda et al. 2015; Mihos et al. 2015; Peng & Lim 2016; Yagi et al. 2016; Gannon et al. 2022), but they have since been observed in a much wider range of environments (van der Burg et al. 2017; Lee et al. 2017, 2020; Marleau et al. 2021; La Marca et al. 2022; Venhola et al. 2022), including in the field (Martínez-Delgado et al. 2016; Román & Trujillo 2017; Leisman et al. 2017; Martín-Navarro et al. 2019; Rong et al. 2020a). While many are observed to be devoid of gas (Martínez-Delgado et al. 2016; Papastergis, Adams & Romanowsky 2017; Román et al. 2019; Junais et al. 2021), more recent observations find gas-rich UDGs (e.g. Leisman et al. 2017; Mancera Piña et al. 2020; Jones et al. 2023). In addition to spanning a wide range of gas fraction and environments, UDGs also broadly span nucleation fraction (Lim et al. 2020).

Given the apparent diversity of UDGs, it has proven particularly difficult to pinpoint a unique formation path that may explain their origin. Several theoretical and numerical studies have pointed to differences between the dark matter haloes that host UDGs and normal dwarfs, suggesting the possibility that UDGs may reside in dark matter haloes with higher-than-average spin (Amorisco & Loeb 2016; Rong et al. 2017; Mancera Piña et al. 2020; Kong et al. 2022; Benavides et al. 2023). Other studies present more baryon-focused formation scenarios. Star formation and feedback processes associated with starburst-driven outflows have the potential to leave the stellar component of galaxies rather extended (e.g. Di Cintio et al. 2017; Chan et al. 2018), although even galaxies passively forming stars have been shown to form UDGs (Tremmel et al. 2020). To add an additional complication in the search for UDG formation, environmental effects, such as tidal heating (Carleton et al. 2019) and tidal stripping (Macciò et al. 2021; Doppel et al. 2021; Moreno

★ E-mail: jessicadoppel@gmail.com

et al. 2022), have also been argued to give rise to UDG-like galaxies. Moreover, combinations of the aforementioned scenarios are also possible (Jiang et al. 2019; Sales et al. 2020), thus an obvious UDG-formation route has yet to emerge.

Constraining the dark matter content of UDGs provides an additional dimension to understanding the origin of UDGs. For example, UDGs with little to no dark matter could suggest a primary formation mechanism of tidal stripping or other processes that preferentially removes dark matter) as a main driver (see e.g. van Dokkum et al. 2018, 2019, 2022; Trujillo-Gomez, Kruijssen & Reina-Campos 2022). At the other extreme, UDGs that inhabit overly massive haloes for their stellar mass could indicate that UDGs may originate as systems originally destined to become large, massive galaxies but where star formation was truncated early on (see e.g. Forbes et al. 2020; van Dokkum et al. 2015b, 2017; Toloba et al. 2023). Between these two extremes, UDGs that reside in dark matter haloes on par with other those of galaxies of similar stellar mass could suggest that UDGs are simply the tail of the surface brightness distribution of normal galaxies, and thus lack a distinct origin (e.g. Conselice 2018; Toloba et al. 2018; Lee et al. 2017, 2020; Saifollahi et al. 2021; Toloba et al. 2023). Illuminating the dark matter content of UDGs is, therefore, a necessary component for pinpointing the – potential spectrum of – formation scenarios through which UDGs may arise and help to solidify their place in our understanding of dwarf galaxies.

Unfortunately, the dark matter content reported thus far for UDGs is as varied as their potential formation scenarios. Observations of luminous, kinematical tracers such as stars (e.g. DF44 (van Dokkum et al. 2017) and DF4 (Danieli et al. 2019) among others), globular clusters (GCs) (see e.g. van Dokkum et al. 2018; Toloba et al. 2018; van Dokkum et al. 2019), and gas (Mancera Piña et al. 2020) suggest that the dark matter haloes of UDGs span the entire range between lacking dark matter (such as DF2 and DF4 in NGC1052,) to residing in haloes with masses far exceeding those expected for their stellar masses (Beasley et al. 2016; Janssens et al. 2022; Gannon et al. 2023; Toloba et al. 2023), with others between these extremes (see e.g. Lee et al. 2017; Toloba et al. 2018; Lee et al. 2020; Saifollahi et al. 2021; Toloba et al. 2023).

For UDGs for which kinematical tracers, such as stars and gas, are unavailable, GCs offer an alternative measure of their halo masses due to their relative ease of observation over large distances and their rather extended spatial distributions. The numerous GCs often associated to UDGs have been interpreted to indicate that they reside in overmassive dark matter haloes (van Dokkum et al. 2015a; Peng & Lim 2016; van Dokkum et al. 2017; Lim et al. 2018, 2020; Danieli et al. 2022; Janssens et al. 2022) if the power-law relation between GC mass and halo mass (see e.g. Peng et al. 2008; Harris, Harris & Hudson 2015) holds for UDGs. However, recent observations from the Coma cluster suggest that, by GC counts, there appears to be two types of UDGs: those that reside in apparently overmassive haloes for their stellar mass, and those that appear to reside in haloes of more typical in mass for dwarf galaxies (Lim et al. 2018; Forbes et al. 2020; Müller et al. 2021; Jones et al. 2023). A better understanding of the theoretical predictions for the dark matter and GC content of gas-poor UDGs in galaxy groups and clusters is needed.

With the high resolution of the TNG50 simulation of the IllustrisTNG suite, it is possible to morphologically define a set of simulated UDGs in the stellar mass range $M_* = [10^{7.5}, 10^9]\,\mathrm{M}_\odot$ with similar structural parameters to observed UDGs (see Benavides et al. 2023, and subsection 2.2 for additional details). Coupled with the recent addition of a catalogue of GCs added to the simulation (Doppel et al. 2023), we can investigate UDGs in conjunction with their GC systems across a variety of environments, ranging from those comparable with massive elliptical systems to those comparable with the mass of the Fornax and Virgo clusters. We can thus make a realistic comparison with the observations of the GC systems of UDGs in these types of environments to provide possible interpretations for these observations and their implications for the dark matter content of UDGs.

In Section 2, we briefly discuss the details of TNG50 as well as the tagging model used to produce its GC catalogue. In Section 3, we discuss how the modelled GC abundances and kinematics compare to observations as well as what, if any, effect environment has on UDGs and their GC systems. In Section 4, we compare mock observations of the GCs and UDGs in TNG50 to observed UDGs, and we use those mock observations to understand the inferred dark matter content of UDGs, both in the presence of contamination in their assigned GC systems as well as other complicating factors. Finally, in Section 5, we provide a short discussion and summary of our results.

2 METHODS

2.1 Simulation

For this study, we use the highest resolution run of the cosmological hydrodynamical TNG50 (Pillepich et al. 2019; Nelson et al. 2019b) simulation – which is part of the larger IllustrisTNG project (Naiman et al. 2018; Pillepich et al. 2018a; Nelson et al. 2018; Springel et al. 2018; Marinacci et al. 2018; Nelson et al. 2019a). TNG50 features a box size of 51.7 Mpc on each side with 2160^3 gas cells and dark matter particles evolved assuming a flat, ΛCDM cosmology consistent with parameters from Planck Collaboration et al. (2016). This configuration results in a mass resolution of, on average, $8.4 \times 10^4\,\mathrm{M}_\odot$ for its baryonic component and $5.4 \times 10^5\,\mathrm{M}_\odot$ for dark matter particles. The gravitational softening length is 288 pc at $z = 0$ for collisionless components.

The baryonic treatment in TNG50 is introduced in detail in (Weinberger et al. 2017; Pillepich et al. 2018b). Briefly, it includes star formation in the dense interstellar medium (ISM), stellar evolution, including chemical enrichment from stars and supernovae; primordial cooling, metal-line cooling, and heating, via background radiation, of gas; additionally, the seeding and growth of supermassive black holes, low and high-accretion AGN feedback, galactic winds, and magnetic fields (Weinberger et al. 2017; Pillepich et al. 2018b).

2.2 Sample of UDGs in groups and clusters

Haloes and subhaloes within the TNG50 simulation are identified using the Friends-of-Friends (FOF, Davis et al. 1985) and SUBFIND (Springel et al. 2001; Dolag et al. 2009), respectively. Using these catalogues, we select the most massive 39 systems at $z = 0$ which span a virial mass range $M_{200} = [5 \times 10^{12}, 2 \times 10^{14}]\,\mathrm{M}_\odot$ (where 'virial' refers to quantities measured within a sphere enclosing 200 times the critical density of the universe). Within such groups and clusters, we study the satellite UDG sample first introduced in Benavides et al. (2023). Simulated UDGs are selected to be in the stellar mass range $M_* = [10^{7.5}, 10^9]\,\mathrm{M}_\odot$– to ensure that there are sufficient stellar particles to resolve the structure of the galaxy. The evolution of these objects are followed using the SUBLINK merger trees (Rodriguez-Gomez et al. 2015).

Inspired by the UDG classification process presented by Lim et al. (2020), wherein UDGs are selected to be 2.5σ outliers in scaling relations between luminosity and surface brightness, mean

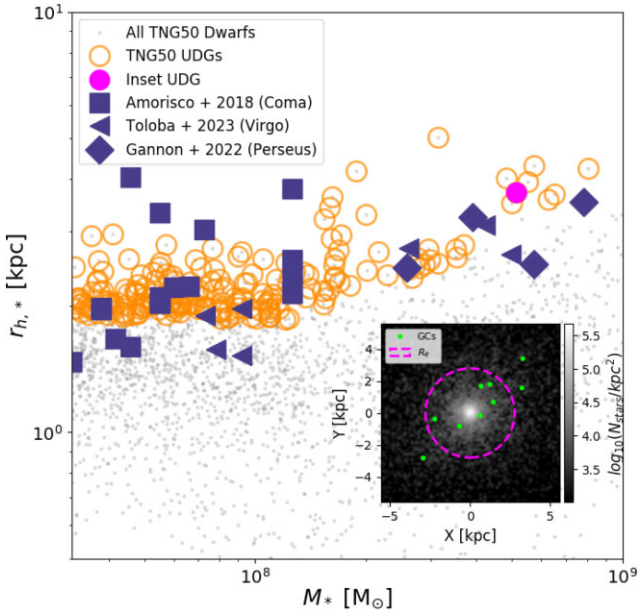

Figure 1. Stellar size ($r_{h,*}$) as a function of stellar mass (M_*) in TNG50 for all dwarf galaxies (grey dots), and for the UDG sample (unfilled orange circles). We show the same for UDGs in the Coma cluster (purple squares, Amorisco et al. 2018), the Virgo cluster (purple triangles Toloba et al. 2023), and the Perseus cluster (purple diamonds, Gannon et al. 2022). The size of observed UDGs has been multiplied by 4/3 (e.g. Hernquist 1990; Wolf et al. 2010; Somerville et al. 2018) to transform it into a 3D measurement (Section 4). Highlighted in pink is the size and mass of the example TNG50 UDG shown in projection in the inset panel, coloured by stellar number density and overplotted with its 2D effective radius, R_e (dotted pink circle), and GC system (lime-green dots). We can see that, where data are available, there is good agreement between the sizes of the observed satellite UDGs in galaxy clusters and the sample of satellite UDGs in TNG50.

effective surface brightness, and effective radius, simulated UDGs are identified as the 5 per cent most extended outliers in the M_*–size relation. These UDGs are shown in Fig. 1, which shows the relation between stellar half-mass radius, $r_{h,*}$, and stellar mass, M_*. These criteria result in UDGs that are roughly consistent with sizes of UDGs in Virgo (purple triangles, Toloba et al. 2023), Coma (purple squares Amorisco et al. 2018), and Perseus (purple diamonds Gannon et al. 2022) clusters, low-density environments (Román et al. 2019; Martín-Navarro et al. 2019; Rong et al. 2020b), as well as other commonly assumed cutoffs to identify UDGs in observations ($R_e \geq 1.5$ kpc and $\mu \gtrsim 24.5$ mag arcsec^{-2} measured within the effective radius of stars (e.g. van Dokkum et al. 2015a)).

As discussed in detail in Benavides et al. (2023), the formation mechanism of UDGs in TNG50 suggests that they inhabit mainly high-spin dark matter haloes, although a subdominant fraction ($\sim$ 10 per cent) of satellite UDGs owe their extended sizes to tidal effects within their groups or clusters. Most importantly, all simulated UDGs in TNG50 formed within dark matter haloes in the range $M_{200} \sim [10^{9.3} - 10^{11.2}]\,M_\odot$ – at $z = 0$ for field UDGs or at infall for satellite UDGs – that are in agreement with expectations from their stellar content. In addition, satellite UDGs are found to be red and quiescent while field UDGs are gas-rich and star-forming, in good agreement with observational results (e.g. van der Burg, Remco F. J. et al. 2016; Lee et al. 2020; Ferré-Mateu et al. 2018; Leisman et al. 2017; Mancera Piña et al. 2020; Jones et al. 2023). Note that our simulations also predict a fraction of quiescent UDGs in the field as a result of backsplash orbits (Benavides et al. 2021) that are not included in our sample as they, by definition, do not reside today within group or cluster haloes.

Satellite UDGs have typically undergone substantial tidal stripping of their dark matter haloes (median mass-loss 80 per cent) but only moderate tidal stripping of their stellar component (10 per cent mass-loss from their peak stellar mass). A total of 195 UDGs are found associated to our simulated groups in TNG50 and are the core sample of the analysis in this paper. In addition, these groups and clusters have 2195 non-UDG dwarfs in the same mass range as our UDGs that might be included when necessary for helpful comparisons. This set of UDGs allows us the first opportunity to study the GC systems of UDGs that reside in realistic group and cluster environments.

2.3 GC catalogue

We use the GC catalogue presented in Doppel et al. (2023), which has been added in post-processing to the 39 most massive galaxy groups and clusters in TNG50, spanning a virial mass range $M_{200} = [5 \times 10^{12}, 2 \times 10^{14}]\,M_\odot$. GCs are tagged to all galaxies in the selected groups and clusters provided they satisfy a maximum stellar mass throughout their history of at least $5 \times 10^6\,M_\odot$ and a minimum of 100 dark matter particles (this latter condition is required to avoid spurious baryonic clumps). All galaxies are tagged at their infall time, which is here defined as the last time the galaxy is its own central. On average, this corresponds to the time at which a galaxy crosses the virial radius of its present-day host halo, but it might be an earlier time if the galaxy joins a smaller halo or group before joining their final host system.

GC candidate particles are selected from the dark matter particles associated to the host galaxy at infall time. Following Lokas & Mamon (2001), we fit an NFW profile (Navarro, Frenk & White 1996)

$$\rho_{\rm NFW}(r) = \frac{\rho^0_{\rm NFW}}{(r/r_{\rm NFW})(1 + r/r_{\rm NFW})^2} \quad (1)$$

to the dark matter component of the galaxy. The scale radius $r_{\rm NFW} = r_{\rm max}/\alpha$, where $r_{\rm max}$ is the radius of maximum circular velocity and $\alpha = 2.1623$ (Navarro et al. 1997).

The GCs are assumed to follow a Hernquist (1990) profile

$$\rho_{\rm HQ}(r) = \frac{\rho^0_{\rm HQ}}{(r/r_{\rm HQ})(1 + r/r_{\rm HQ})^3}, \quad (2)$$

which allows us to control the normalization and radial extension of the tagged GCs. We assign two populations of GCs: a red, metal-rich component of GCs that formed *in situ*, and blue GCs, representative of older, more metal-poor GCs that were accreted into the galaxies. The red GCs are chosen to be more spatially concentrated than the blue GCs, with scale radii $r_{\rm HQ} = 0.5 r_{\rm NFW}$ and $3.0 r_{\rm NFW}$ for red- and blue-GCs, respectively, $\rho_{\rm HQ}$ is chosen to maximize the number of GC candidates.

The GC candidates are then selected in relative energy using the distribution function (Binney & Tremaine 2008)

$$f_i(\epsilon) = \frac{1}{8\pi}\left[\int_0^\epsilon \frac{{\rm d}^2\rho_i}{{\rm d}\psi^2}\frac{{\rm d}\psi}{\sqrt{\epsilon - \psi}} + \frac{1}{\sqrt{\epsilon}}\left(\frac{{\rm d}\rho_i}{{\rm d}\psi}\right)\Big|_{\psi=0}\right], \quad (3)$$

where ρ_i is the density profile of i = (dark matter, red- and blue-GCs), Ψ is the relative gravitational potential, and ϵ is the relative energy. In equally spaced bins of relative energy, a fraction $f_{{\rm HQ},i}/f_{\rm NFW}$, where i = red or blue GCs, of dark matter particles is selected. Inspired by constraints inferred for the Milky Way (Yahagi & Bekki 2005), we implement a cut-off radius of $r_h/3$, where r_h is the total half-mass radius of the halo in question, for the GC candidate particles.

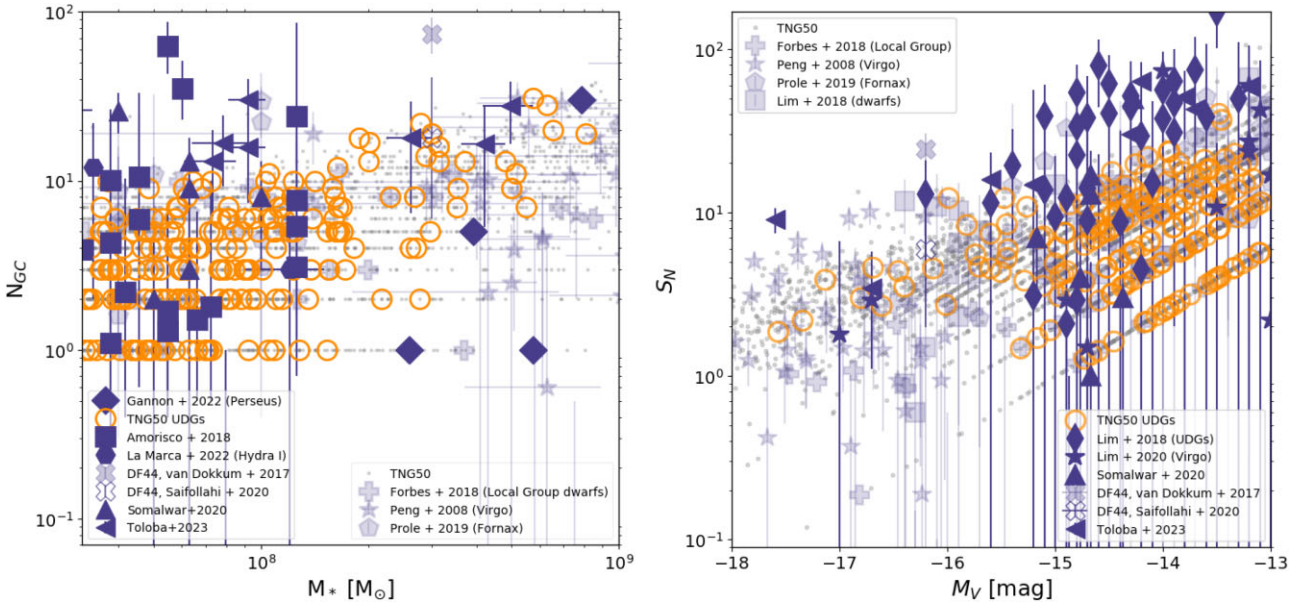

Figure 2. Left: Number of GCs (N_{GC}) as a function of host galaxy stellar mass. All simulated TNG50 satellite dwarf galaxies are shown in translucent grey points, with UDGs highlighted by unfilled orange circles. Observations of GC numbers for normal dwarf galaxies are shown in purple, translucent shapes, and those for UDGs in purple, filled shapes. We can see that while there is a large amount of scatter in the predicted GC numbers for the UDGs of TNG50, the scatter is not as large as what is seen in observed UDGs, particularly those of the Coma Cluster (filled squares). We can see that despite the wide scatter, simulated and observational data follows (on average) similar trends. Right: The specific frequency of GCs (S_N) as a function of host galaxy V-band absolute magnitude (M_V). Following Doppel et al. (2023), we have applied a correction to the V-band magnitude to account for discrepancies between TNG50 and observations for high-mass galaxies. As in the left panel, all TNG50 dwarfs are shown as grey points, UDGs are highlighted by orange circles, observations of S_N for normal dwarf galaxies are shown as translucent purple shapes, and observations of S_N for UDGs are shown as filled, purple shapes. While the simulated UDGs seem to follow well the S_N of observed normal dwarf galaxies and the bulk of observed UDGs, they are unable to reproduce the extreme S_N for many UDGs in the Coma cluster (filled purple diamonds). For both measures of GC abundance in the figures, there is significant overlap between what is predicted by TNG50 and what is observed for the bulk of UDGs; however, we do not predict the most extreme GC systems.

The selected GC candidate particles are assigned masses at infall such that by $z = 0$ those that still remain gravitationally associated to their host follow the M_{GC}–M_{halo} relation from Harris et al. (2015). To make this calibration, we assume that a power-law relation similar to the M_{GC}–M_{halo} relation exists at infall such that

$$M_{GC,inf} = \frac{1}{f_{bound}} M_{GC,z=0} = a_{inf} M_{halo,inf}^{b_{inf}}, \quad (4)$$

where f_{bound} is the fraction of GCs that are still gravitationally bound to their host galaxy at $z = 0$. We find for red- and blue-GCs, respectively, $a_{inf} = 2.6 \times 10^{-7}$ and 7.3×10^{-5} and $b_{inf} = 1.14$ and 0.98.

Since the GC candidates are a much larger set of particles than the observed number of GCs, we subsample a realistic number of GCs from the candidates. This realistic population of GCs follows a Gaussian luminosity function using constraints from Jordán et al. (2007). Individual GC masses are obtained assuming a mass-to-light ratio of 1. GCs are randomly selected from the luminosity function until the total mass of GCs is within $7 \times 10^3\,M_\odot$ (the assumed minimum mass of one GC) of the total calibrated infall mass. The realistic subsample of GCs is followed to $z = 0$ and constitutes the GCs we consider in this work.

Doppel et al. (2023) shows that this method reproduces the available observational constraints in number, specific frequency, and GC occupation fraction over a wide range of masses, including dwarfs. In this paper we focus on the specific predictions of this GC catalogue for the particular case of UDGs in galaxy groups and clusters. By design, our GC tagging method is able to capture the range in GC numbers and kinematics that is expected due solely to variations in the dark matter haloes of UDGs at infall, being an excellent tool to guide the interpretation of current observations.

3 GC ABUNDANCE AND KINEMATICS IN UDGS

We show in Fig. 2 the predicted GC number (N_{GC}, left panel) and GC specific frequency (S_N, right panel) for satellite dwarf galaxies in TNG50 compared to observational constraints. Specific frequency is defined as the number of GCs per unit luminosity normalized to a galaxy with V-band magnitude $M_v = -15$ as follows (Harris & van den Bergh 1981)

$$S_N = N_{GC} 10^{0.4(M_V+15)} \quad (5)$$

Overall, we find a good agreement between all simulated dwarfs in groups and clusters in TNG50 (grey dots) and a compilation of observational data (purple symbols) including normal dwarfs (translucent purple shapes Peng et al. 2008; Forbes et al. 2018; Lim et al. 2018; Prole et al. 2019) and UDGs (filled purple shapes van Dokkum et al. 2017; Amorisco et al. 2018; Lim et al. 2018, 2020; Somalwar et al. 2020; Saifollahi et al. 2021; Gannon et al. 2022).

Fig. 2 indicates that simulated UDGs (unfilled orange circles) display GC numbers that overlap well with the majority of available observations of UDGs (left panel), including systems in low-mass groups (Somalwar et al. 2020) but also high-density environments like Coma (Amorisco & Loeb 2016; Gannon et al. 2022). We note, however, that extreme UDGs with $N_{GC} > 30$ are not present in our simulated catalogue but seem to be present in observations.

This result is not entirely unexpected: all UDGs in TNG50 populate dwarf haloes in the mass range $M_{vir} = [2 \times 10^9, 2 \times 10^{11}]\,M_\odot$

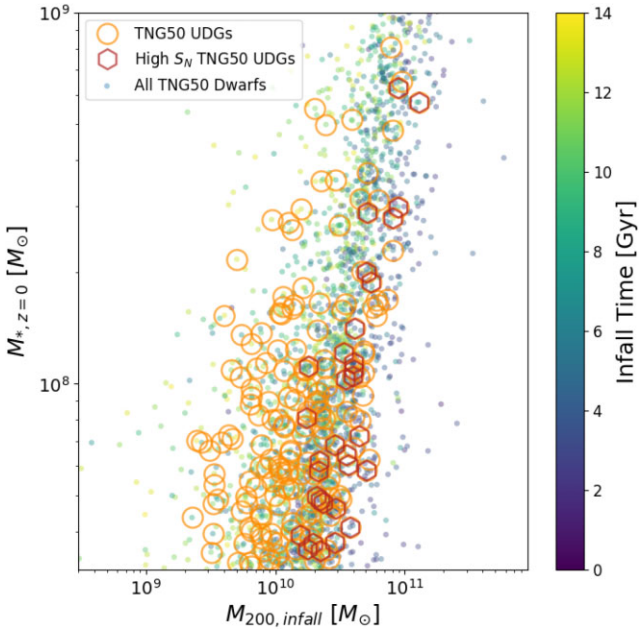

Figure 3. Stellar mass at $z = 0$ ($M_{*,z=0}$) versus virial mass at infall ($M_{200,\,\mathrm{infall}}$) for satellite galaxies in the mass range explored. Symbols are colour-coded by their infall time in Gyr, such that yellow coloured points correspond to a recent infall and bluer points correspond to an earlier infall. UDGs are highlighted by orange circles. We highlight with red hexagons UDGs with the highest S_N in our sample (top 15 per cent of S_N at fixed M_V). These more extreme UDGs tend to have earlier infall times and more massive haloes than their less extreme counterparts..

at infall (using the last time a halo is a central as the definition of infall time, Doppel et al. 2023), and their GC content is a reflection of this prediction. The specific frequency of GCs for these galaxies is shown on the right panel of Fig. 2 and confirms a similar trend: while there is good overlap for many of the simulated UDGs in TNG50, very extreme values with $S_N \gtrsim 50$ are not produced in our simulated sample but exist in systems like the Virgo or Coma clusters (Lim et al. 2018, 2020).

Identifying GCs that are associated to a given galaxy in observations is not without challenge, a subject we return to in Section 4. The iconic UDG DF44 is a good example (van Dokkum et al. 2016). Originally thought to host nearly 100 GCs (van Dokkum et al. 2016), it has been now estimated to have only ∼20 GCs (Saifollahi et al. 2021). If we take the latest measurements as correct, our simulated UDGs are a good representation of galaxies like DF44. Alternatively, if earlier estimates are found to hold, then we do not find DF44 analogues in our sample. The example set by DF44 perhaps warrants a closer look into observed galaxies with very extreme GC content.

Despite the lack of direct analogues to the most extreme observed UDGs in terms of GC number, simulated GC systems encouragingly span a relatively wide range of GC contents, in good agreement with observational claims (e.g. Lim et al. 2018, 2020; Toloba et al. 2023). Of particular interest are those with the largest numbers of GCs (or specific frequency) at any given mass (or luminosity). A closer look to the set of TNG50 UDGs in the top 15 per cent of GC number and specific frequency at fixed stellar mass (and M_V) reveal that these UDGs tend to reside in higher mass – albeit still dwarf-mass – haloes at infall (Fig. 3, where high S_N UDGs are highlighted in red).

Interestingly, this bias towards higher mass haloes for more extreme UDGs is linked to earlier infall times than their less extreme counterparts. This is illustrated clearly with the colour coding of symbols in Fig. 3. This finding is similar to our previous results exploring the GC content of normal dwarfs in the Illustris simulations (Ramos-Almendares et al. 2020). More specifically, at fixed z=0 stellar mass, galaxies with early infall times are biased towards higher halo mass due to the time evolution of the M_*–M_{halo} relation with redshift. Larger halo masses imply a larger number of GCs assigned at infall. In addition, galaxies that infall earlier stop forming stars earlier, meaning that they have passively evolved their stellar population becoming fainter in V-band magnitude and consequently increasing their specific frequency. In TNG50, we find a median infall time $t_{\mathrm{inf}} \sim 6.1$ Gyr for our large GC content UDGs compared to $t_{\mathrm{inf}} \sim 8.1$ Gyr for the rest of the UDG sample.

As with GC content, the velocity dispersion of observed UDGs has been shown to span a wide range. From the popular DF2 and DF4 galaxies associated to NGC1052, whose velocity dispersions ($\sigma < 10\,\mathrm{km\,s^{-1}}$) are so low that they are consistent with no dark matter at all (e.g. van Dokkum et al. 2018; Danieli et al. 2019) to UDGs nearing $\sigma \sim 100\,\mathrm{km\,s^{-1}}$, compatible with haloes so massive that could in theory host MW-like galaxies. Of particular interest is the recent study by Toloba et al. (2023), which represents the first systematic study of the GC kinematics of UDGs in the Virgo cluster. Half of their sample (5 out of 10) shows velocity dispersion $\sigma \geq 50\,\mathrm{km\,s^{-1}}$ measured within 1.5–2 kpc projected radii, making them consistent with inferred halo masses $M_{\mathrm{halo}} \geq 10^{12}\,\mathrm{M_\odot}$– on par with that of the MW (see fig. 9 from Toloba et al. 2023). The authors also report at least one UDG that is also consistent with having no dark matter, which seems to be tied to the ongoing tidal disruption of that particular UDG, partially explaining some of the diverse σ values in the sample.

We show the measurements presented in Toloba et al. (2023), along with a compilation of other available velocity dispersions for observed UDGs in Fig. 4 (purple shapes). The GC velocity dispersion of simulated UDGs in TNG50 are shown with unfilled orange circles. Following Doppel et al. (2021), we have estimated GC velocity dispersion for these systems following an Markov Chain Monte Carlo (MCMC) method with a Jeffreys prior on the dispersion itself, as this method was found to be the most adequate to estimate σ with a small number of tracers (see Appendix A for a brief summary of the method). The error bars on the orange circles show the 25 per cent-75 per cent spread in the velocity dispersion from the PDF stochastically generated via the MCMC method. This is analogous to the way that velocity dispersions were calculated for the GC systems of Virgo-cluster UDGs (Toloba et al. 2023, among others). We include the dispersion of other UDGs in the literature derived from GC kinematics (NGC1052-DF2, van Dokkum et al. 2018), stellar kinematics (DF44, van Dokkum et al. 2019), and stellar spectra – DFX1 (van Dokkum et al. 2017), DGSAT-1 (Martínez-Delgado et al. 2016; Martín-Navarro et al. 2019), UDG7 (Chilingarian et al. 2019), UDG1137+16 (Gannon et al. 2021), and UDGs from the Perseus cluster (Gannon et al. 2022). This set of observed UDGs are selected here to be all consistent with the UDG definition presented by Lim et al. (2020), in that they are outliers of more than 2.5σ in one of the scaling relations between luminosity and surface brightness, mean effective surface brightness, and effective radius.

Encouragingly, the range of GC velocity dispersions predicted by the tagged GCs in TNG50 agrees well with the bulk of observed values for UDGs, in particular for objects with normal-dwarf velocity dispersions such as DFX1, UDG7, UDG1137+16, several Virgo UDGs, and DF44. About half of the UDGs with available velocity measurements are consistent with a dark matter content of a dwarf-mass halo – in agreement with predictions from our UDG sample in

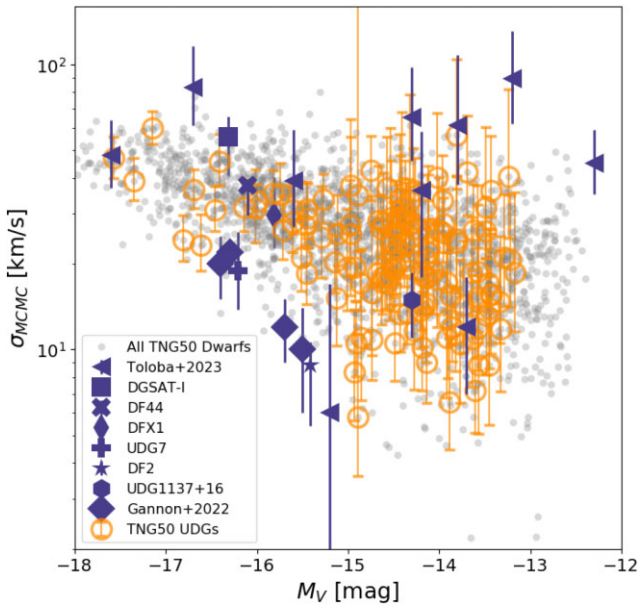

Figure 4. Kinematics of the GC systems of dwarf galaxies in TNG50 calculated via a MCMC method with as Jeffreys prior plotted against host galaxy V-band magnitude, M_V. UDGs in TNG50 are highlighted with orange circles with errorbars representing the 25th–75th percentiles from the PDF generated stochastically by the MCMC method (see Appendix A). All dwarf satellites from TNG50 are shown as grey points. We show observations of GC kinematics from UDGs coming from various studies as large, solid, and purple shapes. We find a wide range of UDGs represented in the literature, with some having dispersions that put them in the range of 'normal' dwarf galaxies, some with dispersions that put them in the dark matter deficient category. Other observed UDGs sit above what is predicted by TNG50, suggesting that they reside in rather over-massive haloes. We note that much of the scatter $\sigma_{\rm MCMC}$ for the UDGs in TNG50 is due to the presence of few GC tracers, making many of the lower scattering points the product of small number statistics. UDGs and their GC systems in TNG50 thus appear to be kinematically indistinguishable from normal dwarf galaxies. Large σ values seem underrepresented in our sample compared to measurements in the Virgo cluster (Toloba et al. 2023).

TNG50. Moreover, the GC velocity dispersion of simulated UDGs overlaps well also with non-UDG dwarf satellites in TNG50 (grey dots). This is indeed expected from the formation scenario of UDGs in this simulation, which place them in dwarf dark matter haloes consistent with the non-UDG sample (although with a small bias towards higher mass, e.g. Benavides et al. 2023).

Interestingly, we also see in Fig. 4 several UDGs and dwarfs from TNG50 that show $\sigma_{\rm MCMC} < 10\,{\rm km\,s^{-1}}$, reminiscent of dark matter free UDGs such as NGC1052-DF2. A closer inspection of this simulated analogues to NGC1052-DF2 show that several have undergone a rather significant amount of dark matter stripping (as was found in Doppel et al. 2021). However, much of the scatter in the lower σ UDGs arises from having only 3–5 GCs to recover the potential of their host halo. As Doppel et al. (2021) showed, using a Jeffreys prior for a low number of tracers performed well in recovering dynamical mass in the median of the sample, but with a large galaxy-to-galaxy scatter. This is a large contributor to the source of kinematic analogues to NGC1052-DF2 in TNG50 and highlights the importance of having a sufficient number of tracers to make accurate individual dark matter mass estimates (see also Toloba et al. 2016; Toloba et al. 2018; Martin et al. 2018; Laporte, Agnello & Navarro 2019; Hughes et al. 2021).

Alternatively, UDGs with high GC velocity dispersion, $\sigma_{\rm MCMC} > 50\,{\rm km\,s^{-1}}$, are less common in our simulated sample compared to available observational constraints. A closer inspection of our high velocity cases shows a similar situation as described earlier: they tend to have 3–5 dynamical tracers and scatter upwards of their true velocity dispersion (as measured from their mass content within R_e). High-dispersion objects are interesting because they do not conform to the expectations of dark matter content given their luminosity. Several candidates have been hinted at in observations including, for example, objects like DGSAT-1 (Martínez-Delgado et al. 2016) and NGVSUDG-09, NGVSUDG-05, NGCSUDG-11, NGVSUDG-19, NGVSUDG-20, and NGVSUDG-A04 from the Toloba et al. (2023) study of UDGs in Virgo. These are often interpreted as 'failed' massive haloes that were destined to form a galaxy more comparable to the Milky Way, but stopped forming stars much earlier than expected, resulting in an overly massive halo given its stellar mass (van Dokkum et al. 2015a; Peng & Lim 2016; van Dokkum et al. 2017; Lim et al. 2018; Lahén et al. 2020; Danieli et al. 2022; Janssens et al. 2022). Calculations presented in Toloba et al. (2023) show that haloes more massive than $M_{200} \sim 10^{12}\,{\rm M_\odot}$ are necessary to explain the kinematics of the large-$\sigma_{\rm MCMC}$ UDGs. Such 'failed' galaxies are not present in the simulated UDG sample in TNG50.

This finding may have different explanations. The most straightforward one is that there may be a legitimate disagreement between theory and observation, implying that the physical mechanisms to form such massive failed galaxies is missing from cosmological simulations (as no other simulation has reported successfully forming such dark matter dominated objects to date) and from our understanding of galaxy formation. Alternatively, the origin of the large velocity dispersion in observed UDGs may be attributed to the presence of observational errors (which are not considered in Fig. 4), interlopers and/or observational biases which are not currently included when comparing with theoretical predictions. We use our simulated GC catalogue to more closely address whether contamination alone may explain the observed UDGs with large inferred dark matter halo masses.

4 EFFECTS OF INTERLOPERS ON THE GC VELOCITY DISPERSION OF UDGS

The analysis of the simulated UDGs and their GCs in Section 3 assumes that only the gravitationally associated GCs are taken into account when estimating GC numbers and kinematics. For the case of the TNG50 simulations, we use information from SUBFIND to determine whether or not a GC is gravitationally bound to a given UDG. However, this is not possible in observations, where assigning membership to GCs nearby a galaxy of interest becomes an additional challenge.

In the specific sample from the Virgo cluster, where most of the available kinematical constraints on UDGs exist (Toloba et al. 2018, 2023), GC membership is based on a combined criteria in projected distance to the host galaxy: $R < 7R_e$, with R_e the effective radius of the host UDG, and an additional restriction on the relative line-of-sight velocity between the candidate GC and the UDG, set to be less than $200\,{\rm km\,s^{-1}}$. We can use our simulated catalogues to evaluate the degree to which the selection effects and specific choices applied in observed samples may lead to the possible inclusion of interloper GCs, biasing the velocity or mass estimate for some UDGs.

We construct mock observations of our simulated samples by projecting all groups and clusters in a given direction and applying a similar selection criteria as described in Toloba et al. (2023). By doing so, we are considering the top two possible contamination sources: (i)

GCs associated to other galaxies that are near the UDG in projection and (ii) GCs in the diffuse intracluster GC component (ICGCs). Assuming that the luminous mass of the UDGs is distributed roughly spherically, we make the conversion between 3D stellar half-mass radius ($r_{h,*}$ and projected effective radius (R_e) using $R_e = 3/4 r_{h,*}$ (e.g. Hernquist 1990; Wolf et al. 2010; Somerville et al. 2018).

For illustration, Fig. 5 shows 8 examples of simulated UDGs and their GCs in our sample. These examples are chosen to showcase different levels of contamination by interlopers and are not a random selection of UDGs in our sample. The stellar number density of the UDGs and their surroundings is shown by the background greyscale, and the GCs that fall in projection within the frames are represented by different symbols (see legend). We label them satellite-1 through -8, or S1-S8 for short, with a label on the upper right-hand corner of each panel. We can find UDGs in relatively isolated surroundings (such as S1, S2, S5, and S8) as well as to those in crowded or obviously with interlopers from several companion galaxies in projection (S3, S4, S6, and S7).

Further, we apply the selection criteria in GC radial velocity, $v_{\rm proj,\,GC}$. Fig. 6 shows this for the 8 examples discussed earlier. For convenience, we centre the GC velocities on that of the host UDG. Following Toloba et al. (2023), we consider GCs within $7R_e$ of their host galaxy and within $\pm 200\,{\rm km\,s^{-1}}$ of the velocity of their host galaxy as bound to the host galaxy (purple box). GCs that would be selected as members by this method are lime green dots highlighted by large purple circles, while those outside of the selection box are shown in lime green. We use our simulation to obtain additional information for each GC. Those known to be gravitationally bound to the UDGs (based on SUBFIND information) are outlined by dark-blue squares. GCs that belonged to the UDG but have now been tidally stripped are outlined by magenta stars, and those outlined by sky blue hexagons are GCs associated to other subhaloes. Lime green dots without any outlining shape belong to the intracluster GC component. In all panels we quote, on the upper-right corner, the actual 1D velocity dispersion calculated with all bound GCs ($\sigma_{\rm true}$) along with the corresponding velocity dispersion computed using the objects within the selection box ($\sigma_{\rm obs}$). We emphasize that, similar to observational samples, the velocity dispersion determination is computed using an MCMC method assuming a Jeffreys prior (see Appendix A for details).

In general, we find that this simple selection criteria works rather well in most cases considered, with a few exceptions. We can see that for all eight featured UDGs, most of the GCs gravitationally bound to the galaxy are recovered by this selection method, with the exception of S2 and S7, which are missing 5 and 1 associated GCs, respectively, when the selection criteria are applied. Note that in neither case does this matter for the velocity dispersion measured, which remains very close to the true value even when missing a few GCs (upper-right corner of each panel).

As expected, the inclusion of velocity information is critical to remove GC interlopers. For example, S3 and S6 in Fig. 5 have obvious contamination ongoing due to the overlap in projection with other satellites in the group. We can see in Fig. 6 that the addition of velocity removes the interlopers associated with S3. However, this is not the case for S6, where GCs bound to the companion galaxy fulfill the criteria of membership due to chance alignment in the velocities. This results, for the specific case of S6, in a factor 2 overestimation of the velocity dispersion inferred: using the GCs within the selection box results in $\sigma_{\rm obs} \sim 50\,{\rm km\,s^{-1}}$ whereas the truly associated GCs are moving with $\sigma_{\rm act} \sim 24\,{\rm km\,s^{-1}}$.

While the case of S6 demonstrates that care must be exercised when dealing with projected data, it presents a type of contamination that observational studies will avoid unless absolutely necessary. In fact, none of the UDGs considered in the sample of Toloba et al. (2018) or Toloba et al. (2023) contains other galaxies in projection on the line of sight that are brighter than $M_V \sim -13$; therefore, they are not luminous enough to have GCs that pose the risk of significantly contaminating the GC sample (see section 5.1 of Toloba et al. 2023). In what follows, we choose to ignore contamination from GCs associated to other subhaloes, as observational studies would purposely remove such complicated systems from their samples.

However, a more subtle case is that of S8 in our sample. S8 is seemingly isolated, but several intracluster GCs fall within the selection box, artificially enhancing the velocity dispersion measured by a factor of $\sim$3. This galaxy would be inferred to inhabit a massive dark matter halo with $\sigma_{\rm GC} \sim 100\,{\rm km\,s^{-1}}$, while in reality it inhabits a dwarf-mass halo with $\sigma_{\rm true} \sim 35\,{\rm km\,s^{-1}}$. This presents a concrete example where an otherwise relatively normal UDG could be kinematically mistaken as bearing an overly massive halo.

Are cases like S8 common in our sample? For that, we need to evaluate how often contamination from the intracluster component sneaks into the selection box. We quantify this in Fig. 7. We show, as a function of the number of GCs within the selection box in our UDGs, $N_{\rm GC,Selected}$, the ratio of the measured velocity dispersion (including intracluster interlopers) and the true value (computed with only bound GCs according to SUBFIND). For the vast majority of simulated UDGs the velocity dispersion estimate remains within 20 per cent of its true value, suggesting that it is not likely that interlopers will play a dominant effect in the majority of UDG measurements. However, for systems with less than 10 GCs, the inclusion of intracluster contamination may cause overestimation of the velocity by factors 2–10. The median and percentiles show, however, that it is statistically much more likely to remain within 15 per cent of the true value.

4.1 Can intracluster GCs then explain the high-incidence of large velocity dispersion UDGs found in Virgo?

A close inspection of Fig. 6 shows that interlopers tend to have the largest distances and largest velocity difference with the central galaxy (yet still remaining within the selection box). We have re-analysed the velocity dispersion of the most extreme 'failed galaxies' example in Virgo from Toloba et al. (2023) removing the furthest GC or the largest velocity difference GC and found no significant change in the estimates of their velocity dispersion or dynamical mass. These include NGVSUDG-05, NGVSUDG-09, NGVSUDG-11, NGVSUDG-19, NGVSUDG-20, and NGVSUDG-A04 using the nomenclature of the original paper. The most extreme variation is for NGVSUDG-09, which changes from $\sigma = 83^{+33}_{-22}\,{\rm km\,s^{-1}}$ to $\sigma = 60^{+25}_{-15}\,{\rm km\,s^{-1}}$. While these values are still statistically consistent, the median velocity dispersion is brought more in line with TNG50 UDGs. Worth noticing, NGVSUDG-19 has only 3 GCs members identified, so it is necessary to proceed with caution regarding this particular target.

In order to evaluate the possibility of contamination in the Toloba et al. (2023) sample more closely, we restrict now our simulated sample to only UDGs outside of $0.1R_{\rm vir}$ from their host cluster and with $N_{\rm GC,\,Selected} \geq 5$, (only excluding 1 target from Toloba et al. 2023). A total of 242 UDGs satisfy these criteria when using 3 different projections – along the x-, y-, and z- axis of our 39 groups and clusters in TNG50. We derive from these mock projections: the corresponding 1D MCMC velocity dispersion, the half-number

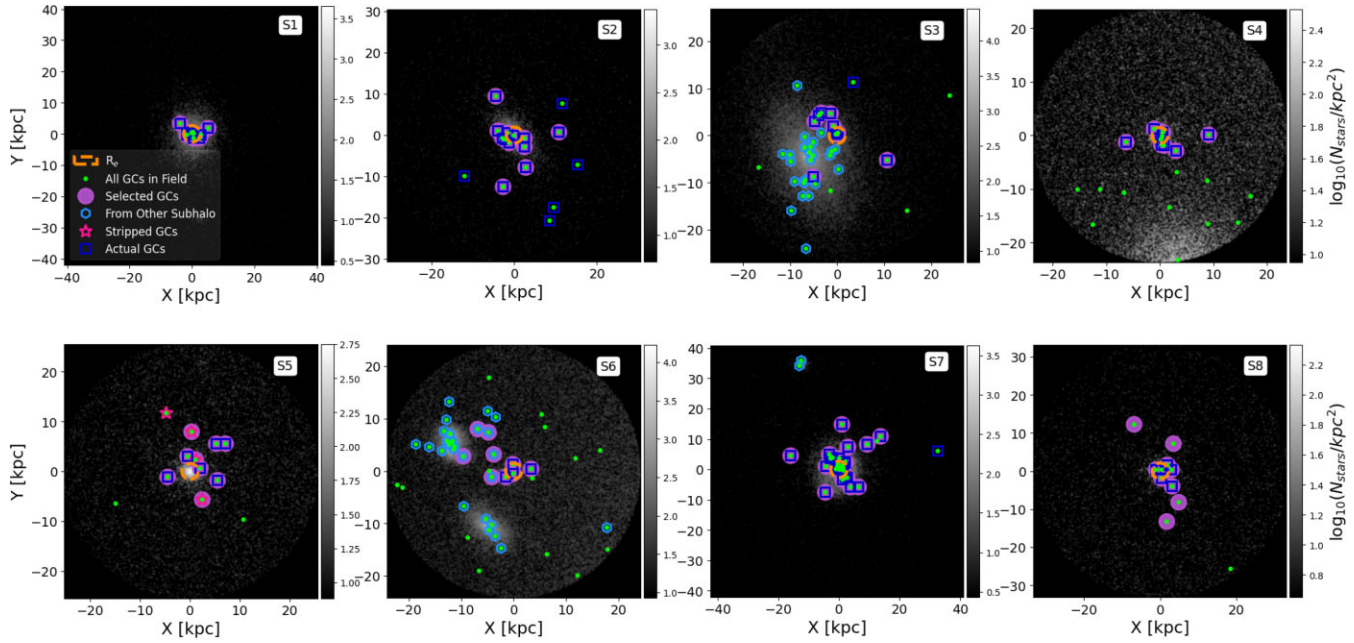

Figure 5. Mock X–Y projections of stars (background greyscale, coloured by the number density of stars in each bin) and GCs (lime-green points) within $16R_e$ of 8 UDGs within TNG50. We name the satellites S1-S8 as annotated in the upper right corner of each panel. The UDGs shown are selected to have at least 8 GCs in within $16R_e$ of the host UDG and to display a range of scenarios from quite easy to surprisingly difficult for selecting bound GCs (see Section 4). GCs that would be considered associated in observations are highlighted with an underlying large purple circles, those that belong to other subhaloes by sky blue hexagons, those that are tidally stripped by pink stars, and actual GCs bound to the subhalo by dark blue squares. For reference, we show the R_e of each UDG as dashed, orange circles. Several UDGs, namely S1, S2, S5, and S8 are quite isolated, with the rest having one or more other galaxy in the field of view. From spatial information alone, determining GC boundness is not straightforward.

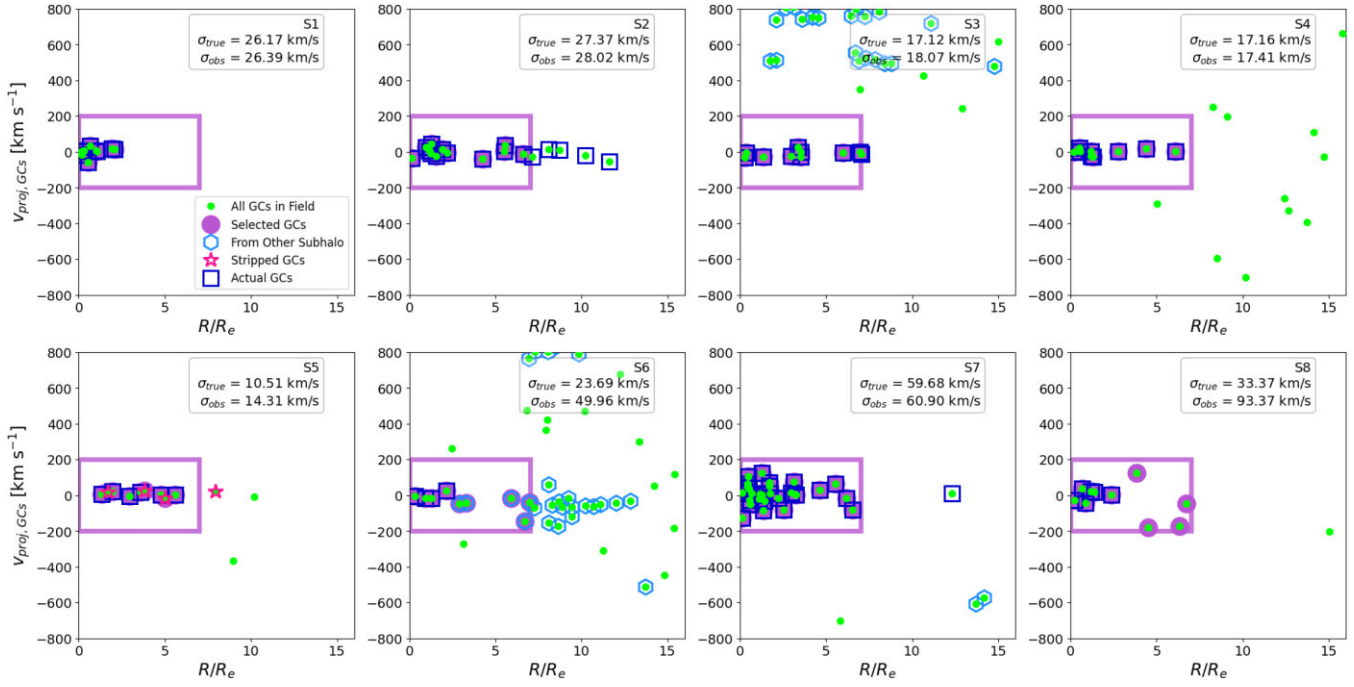

Figure 6. A mock observation of the radial velocity of the GCs associated to the eight UDGs in Fig. 5. GCs are considered members of the galaxy if they fall within $7R_e$ of a given galaxy and their radial velocities are within $\pm 200\,\mathrm{km\,s^{-1}}$ of that of their suspected host galaxy (e.g. within the purple box). All symbols correspond to GCs in the field of view, colour coded according to the legend on the upper left panel. Overall, assigning GCs based on kinematics is a powerful tool, but it can fail. S8 represents an interesting case in which interloper GCs from the intracluster component are flagged as members and substantially increase the estimated velocity dispersion.

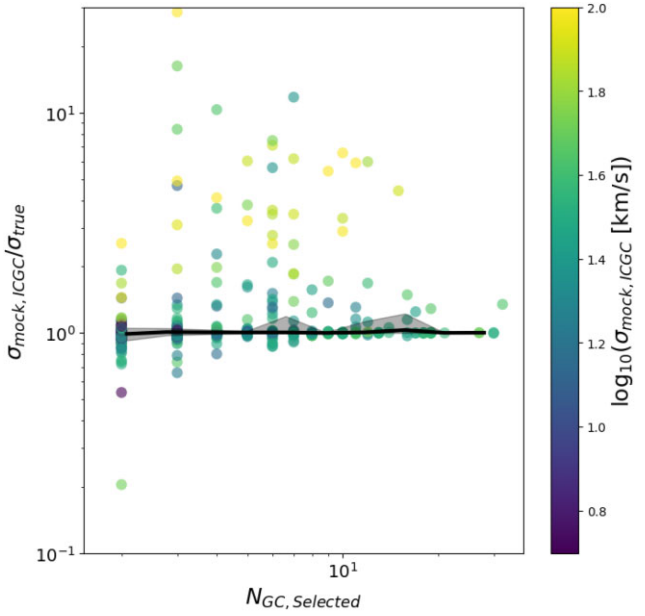

Figure 7. The ratio of the GC velocity dispersion measured via mock observations, $\sigma_{\rm mock,\,ICGC}$. to the actual GC velocity dispersion, $\sigma_{\rm true}$ as a function of total GCs selected, $N_{\rm GC,\,Selected}$ via the method described in Section 4, with points coloured by $\log_{10}(\sigma_{\rm mock,\,ICGC})$. We can see that for small GC numbers, the $\sigma_{\rm mock,\,ICGC}$ can be greatly inflated from its true value, especially from intracluster GC contaminants. For most galaxies, as shown by the median and 25 per cent–75 per cent spread (black line and shaded region), the mock observations do not pick up a significant number of interloping intracluster GCs in the mock observations, leading to an overall median $\sigma_{\rm mock,\,ICGC}/\sigma_{\rm true} \sim 1$.

radius of the GCs, and the dynamical mass at half-number radius following Jeans modelling as in Wolf et al. (2010).

Fig. 8 shows the inferred masses for this subsample of simulated UDGs as a function of the half-number radius of their selected GCs. The left-hand panel of Fig. 8, shows simulated UDGs that fulfill the requirement and have no contamination from interloper GCs. For reference, the grey lines represent the mass profiles corresponding to NFW profiles with halo masses $M_{200} = 10^{10}$, 10^{11}, and 10^{12} $\rm M_\odot$ and a concentration $c = 10$. As shown by the median and dispersion of the brown points, the recovered mass follows quite closely the expected halo mass $M_{200} \sim 10^{11}\,\rm M_\odot$ (dashed grey line) for this simulated objects. For comparison in Fig. 8, we include the inferred dynamical mass of several observed UDGs that are derived from their reported velocity dispersions (whether from GCs, stars, or stellar spectra) and half number radii (GCs) or effective radii (stars) via dynamical mass estimation (see Wolf et al. 2010).

Conversely, contamination by GCs along the line of sight can introduce some scatter upwards of the expected dark matter mass content. This is shown in the right panel of Fig. 8, where simulated UDGs with 5–9 selected GCs with at least one interloper are shown in grey open circles while those with 10 or more (including interlopers) are indicated by black open circles. While a large fraction of the points are still consistent with the expected mass content of simulated UDGs in TNG50 at infall, $M_{200,\,\rm infall} \sim 10^9 - 10^{11}\,\rm M_\odot$ (Benavides et al. 2023), there is a much larger incidence of grey circles near and above the $M_{200} \sim 10^{12}\,\rm M_\odot$ line, suggesting that low numbers of kinematical tracers may play a role in the appearance of overmassive haloes. Such is the case of S8 introduced before in Figs 5 and 6, highlighted in pink, which moves from a true mass–density consistent with the dashed line ($M_{200} \sim 10^{11}\,\rm M_\odot$) to its inferred density more consistent with a MW-mass halo with $M_{200} > 10^{12}\,\rm M_\odot$.

Worth discussing is also the case of S7, highlighted on the left-panel of Fig. 8 as the purple diamond. As shown in Fig. 6, S7 does not include contamination by GC interlopers in its mocked GC sample (and the reason we display it on the left-panel of Fig. 8). Yet its inner density is high and consistent with MW-like haloes both when applying the mock selection in projection or when considering all bound GCs according to SUBFIND. We have checked that this high density is not the result of an overly massive halo but instead corresponds to a dwarf-mass halo with a larger-than-typical concentration. The virial mass before infall for S7 is $M_{200} \sim 9 \times 10^{10}\,\rm M_\odot$. This galaxy is a good reminder that variations in concentration may also drive some of the scatter in the inferred dark matter content of UDGs, a possibility briefly discussed in Gannon et al. (2022).

Given these results, can intracluster GCs explain the high-incidence of large velocity dispersion UDGs found in Virgo? Within the range of galaxy groups and clusters that we can explore with TNG50, we find that contamination from intracluster GCs is unlikely to explain the high incidence of high-mass UDGs in Virgo reported recently by Toloba et al. (2023). Only a handful of simulated UDGs are driven close to the $M_{200} \sim 10^{12}\,\rm M_\odot$ line due to contamination effects, with only 9.5 per cent of UDGs with 5 GCs or more showing velocity dispersion overestimation by a factor of 2 or more in the mock observations. However, a factor to keep in mind is that even the most massive simulated galaxy cluster in TNG50 (Group 0, $M_{200} = 1.87 \times 10^{14}\,\rm M_\odot$) is on the the low end of mass estimates for the Virgo cluster ($M_{200} \sim 2 - 9 \times 10^{14}\,\rm M_\odot$, Karachentsev & Nasonova 2010; Weinmann et al. 2011), with the remainder of our groups in the simulated sample being lower mass. For our most massive cluster, we predict a total of 34 231 GCs with $M \geq 7 \times 10^3\,\rm M_\odot$, which is on par with what is expected for the GC number density of the M87 subgroup in Virgo (e.g. Lee, Park & Hwang 2010; Durrell et al. 2014), but is about a factor of two lower than the combined estimate when considering also the M49 subgroup, $N_{\rm GC,\,Virgo} \sim 67\,300 \pm 14\,400$ (Durrell et al. 2014). All of the remaining groups in our simulated sample are less massive and will therefore have less GCs than Group 0. It is therefore possible that chance alignment of ICGCs has a larger impact in the specific case of observations in Virgo than found on average in our study.

5 DISCUSSION AND SUMMARY

We use a catalogue of GCs added to the TNG50 cosmological simulation, introduced in Doppel et al. (2023), to study the population of GCs associated to UDGs with stellar mass $M_* = [10^{7.5}, 10^9]\,\rm M_\odot$ in 39 groups and clusters with $M_{200} = [5 \times 10^{12} - 2 \times 10^{14}]\,\rm M_\odot$. UDGs are selected as outliers in the mass–size relation as presented in Benavides et al. (2023).

UDGs in galaxy groups and clusters in TNG50 are found to form in dwarf-mass haloes with biased-high spins and virial masses between $M_{200,\,\rm infall} = [10^{9.3}, 10^{11.2}]\,\rm M_\odot$. As a result, simulated UDGs have similar GC numbers to those associated with non-UDG dwarfs of similar stellar mass. We find between 1–30 GCs bound to the simulated UDGs, with only 12 UDGs having no GCs at all. This seems in agreement with observed UDGs, which show a large spread in GC content (Amorisco et al. 2018; Lim et al. 2018, 2020; Somalwar et al. 2020; Gannon et al. 2022; La Marca et al. 2022; Toloba et al. 2023).

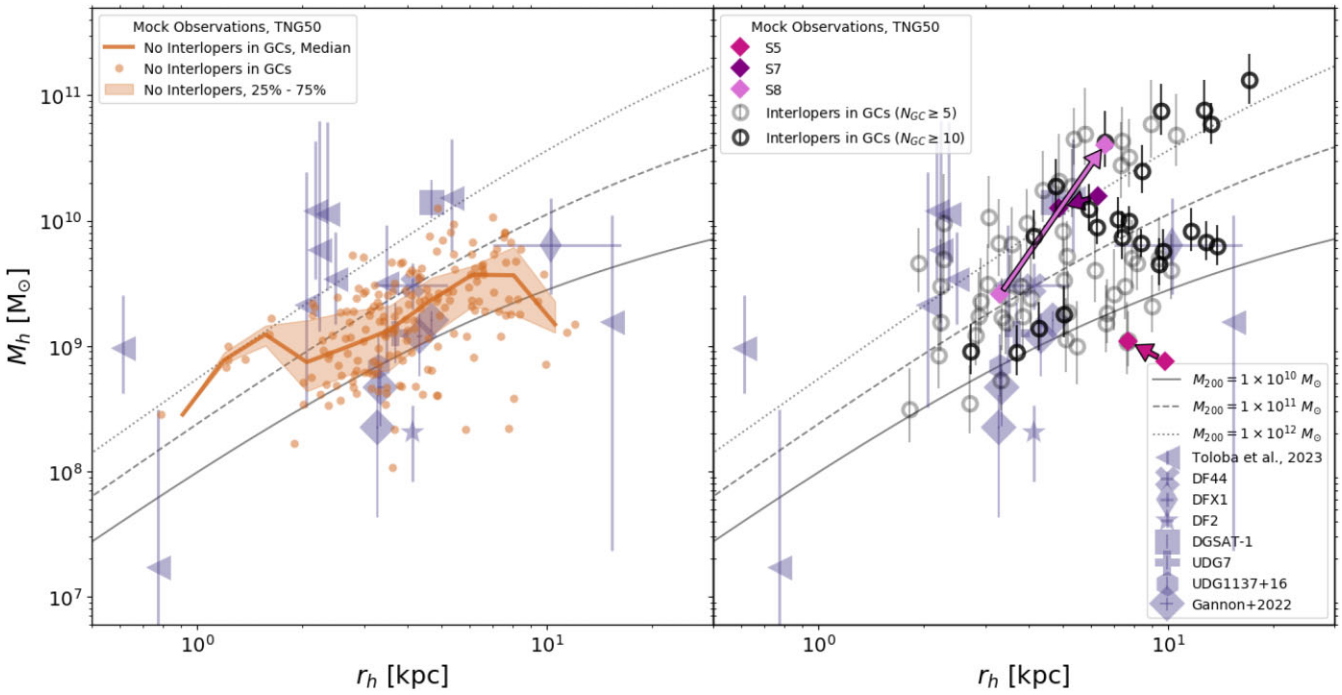

Figure 8. Effects of GC contamination on dark matter mass inferences from GC kinematics. We select simulated UDGs with more then 5 GCs in projected mock observations, and we divide them into those with no GC interlopers (left) and those with interlopers (right). Error bars on the right panel for simulated UDGs correspond to the 25 per cent–75 per cent scatter from their MCMC pdfs. Grey lines show the mass profiles of NFW haloes with concentration $c = 10$ and halo masses $M_{200} = 10^{10}$, 10^{11}, 10^{12} $M_\odot$, to guide the eye. Semi-transparent purple symbols also show current estimates for observed UDGs in the literature. Overall, GCs are good dynamical tracers, but low counts and the possibility of interlopers (right hand) can bias-high the mass estimation. Highlighted are three cases from Fig. 6, S5, S7, and S8, shown by double symbols connected by arrows pointing from M_h estimated without GC interlopers to the case where the mass is estimated using all GCs in projection. In the case of S8 (light pink) it is clear that intracluster GCs result in an overestimation of mass.

However, our sample lacks extreme outliers, with $N_{GC} > 30$, and $S_N > 50$, as some observations suggest (e.g. Peng & Lim 2016; Lim et al. 2018, 2020; Müller et al. 2021). The lack of high specific GC frequency simulated UDGs is ultimately linked to the fact that UDGs in TNG50 all inhabit dwarf-mass haloes, which have low GC numbers according to the scaling assumed in the model. We caution, however, that uncertainties are still important in observations. For example, our predictions fall well below the initial number of ∼100 GCs reported for the iconic DF44 (van Dokkum et al. 2017) but agree very well with its revised value ∼20 in the more recent work by Saifollahi et al. (2021).

As for the GC numbers, we find in general good agreement between the predicted GC velocity dispersion in simulated UDGs and values reported in the literature for observational samples. Our predictions agree well with σ measurements for a number of UDGs, particularly DF44, DGSAT-1, DFX1, UDG7, and several UDGs in the Virgo cluster. However, large velocity dispersion outliers with $\sigma > 50\,\mathrm{km\,s^{-1}}$ such as those found for half of the UDGs studied in the Virgo cluster in Toloba et al. (2023) are not common in our sample.

We can use our simulated GC catalogues to make projected mock observations of our systems and assess whether interloper GCs could affect the observational results. We find that outliers from the intracluster GC component associated to the host galaxy group or galaxy cluster may in some cases impact the velocity dispersion measurement, inflating σ by factors of >2. These cases are, however, rare, in particular when focusing on UDGs with a sufficient number of tracers (GCs).

In agreement with our previous results Doppel et al. (2021), we find 10 or more GCs are needed for robust kinematical measurements. For instance, only 9.5 per cent of cases with more than 10 GCs have velocity dispersions that are overestimated by more than a factor of 2 because of the presence of interlopers. Such cases will suggest dark matter haloes with $M_{200} \sim 10^{12}\,M_\odot$ when in reality they occupy normal dwarf-mass haloes.

We compare our results with the high incidence of observed UDGs with large velocity dispersions reported in kinematical studies of UDGs in the Virgo cluster and conclude that the frequency of contamination in our systems does not explain the large number of UDGs with $\sigma > 50\,\mathrm{km\,s^{-1}}$ in Virgo. A caveat of our study is that groups and clusters included in TNG50 are on average less massive than Virgo, and the incidence of interloper contamination could be higher in more massive systems. We identify some high inferred halo-mass cases in Toloba et al. (2023), such as UDG 19 or 05 and 20, that have 5 GC tracers or less, making them interesting candidates to follow up spectroscopically for confirmation. Ultimately, for UDGs with a low number of identified GC members, measuring their stellar velocity dispersion might be the only avenue to constrain better their true dark matter mass content and, with it, their possible formation path.

ACKNOWLEDGEMENTS

JED and LVS are grateful for financial support from the NSF-CAREER-1945310 and NASA ATP-80NSSC20K0566 grants. ET is thankful for the support from NSF-AST-2206498 and HST GO-15417 grants. DN acknowledges funding from the Deutsche Forschungsgemeinschaft (DFG) through an Emmy Noether Research Group (grant number NE 2441/1-1).

6 DATA AVAILABILITY

The realistic GC catalogues used in this study are available to the public. The catalogues can be downloaded here: www.tng-project.org/doppel22 or as part of the TNG50 public data release (Nelson et al. 2019a).

REFERENCES

Abraham R. G., van Dokkum P. G., 2014, PASP, 126, 55
Amorisco N. C., Loeb A., 2016, MNRAS, 459, 51
Amorisco N. C., Monachesi A., Agnello A., White S. D. M., 2018, MNRAS, 475, 4235
Beasley M. A., Romanowsky A. J., Pota V., Navarro I. M., Martinez Delgado D., Neyer F., Deich A. L., 2016, ApJ, 819, L20
Benavides J. A. et al., 2021, Nature Astron., 5, 1255
Benavides J. A., Sales L. V., Abadi M. G., Marinacci F., Vogelsberger M., Hernquist L., 2023, MNRAS, 522, 1033
Binggeli B., Sandage A., Tammann G. A., 1985, AJ, 90, 1681
Binney J., Tremaine S., 2008, Galactic Dynamics: Second Edition, rev - revised, 2nd edn. Princeton Univ. Press, Princeton http://www.jstor.org/stable/j.ctvc778ff
Bothun G. D., Impey C. D., Malin D. F., 1991, ApJ, 376, L404
Carleton T., Errani R., Cooper M., Kaplinghat M., Peñarrubia J., Guo Y., 2019, MNRAS, 485, 382
Chan T. K., Kereš D., Wetzel A., Hopkins P. F., Faucher-Giguère C. A., El-Badry K., Garrison-Kimmel S., Boylan-Kolchin M., 2018, MNRAS, 478, 906
Chilingarian I. V., Afanasiev A. V., Grishin K. A., Fabricant D., Moran S., 2019, ApJ, 884, L79
Conselice C. J., 2018, Res. Notes Am. Astron. Soc., 2, 43
Dalcanton J. J., Spergel D. N., Gunn J. E., Schmidt M., Schneider D. P., 1997, AJ, 114, 635
Danieli S., van Dokkum P., Conroy C., Abraham R., Romanowsky A. J., 2019, ApJ, 874, L12
Danieli S. et al., 2022, ApJ, 927, L28
Davis M., Efstathiou G., Frenk C. S., White S. D. M., 1985, ApJ, 292, L371
Di Cintio A., Brook C. B., Dutton A. A., Macciò A. V., Obreja A., Dekel A., 2017, MNRAS, 466, 1
Dolag K., Borgani S., Murante G., Springel V., 2009, MNRAS, 399, 497
Doppel J. E., Sales L. V., Navarro J. F., Abadi M. G., Peng E. W., Toloba E., Ramos-Almendares F., 2021, MNRAS, 502, 1661
Doppel J. E. et al., 2023, MNRAS, 518, 2453
Durrell P. R. et al., 2014, ApJ, 794, L103
Ferré-Mateu A. et al., 2018, MNRAS, 479, 4891
Forbes D. A., Read J. I., Gieles M., Collins M. L. M., 2018, MNRAS, 481, 5592
Forbes D. A., Alabi A., Romanowsky A. J., Brodie J. P., Arimoto N., 2020, MNRAS, 492, 4874
Gannon J. S. et al., 2021, MNRAS, 502, 3144
Gannon J. S. et al., 2022, MNRAS, 510, 946
Gannon J. S., Forbes D. A., Brodie J. P., Romanowsky A. J., Couch W. J., Ferré-Mateu A., 2023, MNRAS, 518, 3653
Harris W. E., van den Bergh S., 1981, AJ, 86, 1627
Harris W. E., Harris G. L., Hudson M. J., 2015, ApJ, 806, L36
Hernquist L., 1990, ApJ, 356, L359
Hughes M. E. et al., 2021, MNRAS, 502, 2828
Impey C., Bothun G., Malin D., 1988, ApJ, 330, L634
Janssens S. R. et al., 2022, MNRAS, 517, 858
Jiang F., Dekel A., Freundlich J., Romanowsky A. J., Dutton A. A., Macciò A. V., Di Cintio A., 2019, MNRAS, 487, 5272
Jones M. G. et al., 2023, ApJ, 942, L5
Jordán A. et al., 2007, ApJS, 171, 101
Junais et al., 2021, A&A, 650, 99
Karachentsev I. D., Nasonova O. G., 2010, MNRAS, 405, 1075
Koda J., Yagi M., Yamanoi H., Komiyama Y., 2015, ApJ, 807, L2
Kong D., Kaplinghat M., Yu H.-B., Fraternali F., Mancera Piña P. E., 2022, ApJ, 936, L166
La Marca A. et al., 2022, A&A, 665, 105
Lahén N., Naab T., Johansson P. H., Elmegreen B., Hu C.-Y., Walch S., Steinwandel U. P., Moster B. P., 2020, ApJ, 891, L2
Laporte C. F. P., Agnello A., Navarro J. F., 2019, MNRAS, 484, 245
Lee M. G., Park H. S., Hwang H. S., 2010, Science, 328, 334
Lee M. G., Kang J., Lee J. H., Jang I. S., 2017, ApJ, 844, L157
Lee J. H., Kang J., Lee M. G., Jang I. S., 2020, ApJ, 894, L75
Leisman L. et al., 2017, ApJ, 842, L133
Lim S., Peng E. W., Côté P., Sales L. V., den Brok M., Blakeslee J. P., Guhathakurta P., 2018, ApJ, 862, L82
Lim S. et al., 2020, ApJ, 899, L69
Lokas E. L., Mamon G. A., 2001, MNRAS, 321, 155
Macciò A. V., Prats D. H., Dixon K. L., Buck T., Waterval S., Arora N., Courteau S., Kang X., 2021, MNRAS, 501, 693
Mancera Piña P. E. et al., 2020, MNRAS, 495, 3636
Marinacci F. et al., 2018, MNRAS, 480, 5113
Marleau F. R. et al., 2021, A&A, 654, 105
Martín-Navarro I. et al., 2019, MNRAS, 484, 3425
Martin N. F., Collins M. L. M., Longeard N., Tollerud E., 2018, ApJ, 859, L5
Martínez-Delgado D. et al., 2016, AJ, 151, 96
Mihos J. C. et al., 2015, ApJ, 809, L21
Moreno J. et al., 2022, Nature Astron., 6, 496
Müller O. et al., 2021, ApJ, 923, L9
Naiman J. P. et al., 2018, MNRAS, 477, 1206
Navarro J. F., Frenk C. S., White S. D. M., 1996, ApJ, 462, L563
Navarro J. F., Frenk C. S., White S. D. M., 1997, ApJ, 490, L493
Nelson D. et al., 2018, MNRAS, 475, 624
Nelson D. et al., 2019a, Comput. Astrophys. Cosmol., 6, 2
Nelson D. et al., 2019b, MNRAS, 490, 3234
Papastergis E., Adams E. A. K., Romanowsky A. J., 2017, A&A, 601, 10
Peng E. W., Lim S., 2016, ApJ, 822, L31
Peng E. W. et al., 2008, ApJ, 681, L197
Pillepich A. et al., 2018a, MNRAS, 475, 648
Pillepich A. et al., 2018b, MNRAS, 475, 648
Pillepich A. et al., 2019, MNRAS, 490, 3196
Planck Collaboration et al., 2016, A&A, 594, 13
Prole D. J. et al., 2019, MNRAS, 484, 4865
Ramos-Almendares F., Sales L. V., Abadi M. G., Doppel J. E., Muriel H., Peng E. W., 2020, MNRAS, 493, 5357
Reaves G., 1983, ApJS, 53, 375
Rodriguez-Gomez V. et al., 2015, MNRAS, 449, 49
Román J., Trujillo I., 2017, MNRAS, 468, 4039
Román J., Beasley M. A., Ruiz-Lara T., Valls-Gabaud D., 2019, MNRAS, 486, 823
Rong Y., Guo Q., Gao L., Liao S., Xie L., Puzia T. H., Sun S., Pan J., 2017, MNRAS, 470, 4231
Rong Y., Mancera Piña P. E., Tempel E., Puzia T. H., De Rijcke S., 2020a, MNRAS, 498, 72
Rong Y., Zhu K., Johnston E. J., Zhang H.-X., Cao T., Puzia T. H., Galaz G., 2020b, ApJ, 899, L12
Saifollahi T., Trujillo I., Beasley M. A., Peletier R. F., Knapen J. H., 2021, MNRAS, 502, 5921
Sales L. V., Navarro J. F., Peñafiel L., Peng E. W., Lim S., Hernquist L., 2020, MNRAS, 494, 1848
Somalwar J. J., Greene J. E., Greco J. P., Huang S., Beaton R. L., Goulding A. D., Lancaster L., 2020, ApJ, 902, L45
Somerville R. S. et al., 2018, MNRAS, 473, 2714
Springel V., White S. D. M., Tormen G., Kauffmann G., 2001, MNRAS, 328, 726
Springel V. et al., 2018, MNRAS, 475, 676
Toloba E. et al., 2016, ApJ, 822, L51
Toloba E. et al., 2018, ApJ, 856, L31
Toloba E. et al., 2023, ApJ, 951, 77
Tremmel M., Wright A. C., Brooks A. M., Munshi F., Nagai D., Quinn T. R., 2020, MNRAS, 497, 2786

Trujillo-Gomez S., Kruijssen J. M. D., Reina-Campos M., 2022, MNRAS, 510, 3356
van der Burg, Remco F. J., Muzzin, Adam Hoekstra, Henk, 2016, A&A, 590, 20
van der Burg R. F. J. et al., 2017, A&A, 607, 79
van Dokkum P. G., Abraham R., Merritt A., Zhang J., Geha M., Conroy C., 2015a, ApJ, 798, L45
van Dokkum P. G. et al., 2015b, ApJ, 804, L26
van Dokkum P. et al., 2016, ApJ, 828, L6
van Dokkum P. et al., 2017, ApJ, 844, L11
van Dokkum P. et al., 2018, ApJ, 856, L30
van Dokkum P. et al., 2019, ApJ, 880, L91
van Dokkum P. et al., 2022, ApJL, 940, L9
Venhola A. et al., 2022, A&A, 662, 43
Weinberger R. et al., 2017, MNRAS, 465, 3291
Weinmann S. M., Lisker T., Guo Q., Meyer H. T., Janz J., 2011, MNRAS, 416, 1197
Wolf J., Martinez G. D., Bullock J. S., Kaplinghat M., Geha M., Muñoz R. R., Simon J. D., Avedo F. F., 2010, MNRAS, 406, 1220
Yagi M., Koda J., Komiyama Y., Yamanoi H., 2016, ApJS, 225, 11
Yahagi H., Bekki K., 2005, MNRAS, 364, 86

APPENDIX A: VELOCITY DISPERSION CALCULATION

To calculate the velocity dispersions used in this work, we utilize an MCMC method which takes set of velocities – in this case, the line-of-sight velocities of a UDG's GCs – and stochastically fits the velocity dispersion, σ and the mean velocity, $\bar{v}$, to a Gaussian distribution. We use the following likelihood in our velocity dispersion estimation

$$\mathcal{L} = \prod_{i}^{N_{GC}} \frac{1}{\sigma\sqrt{2\pi}} \exp\left(-0.5 \left(\frac{v_i - < v >}{\sigma} \right)^2 \right), \quad \text{(A1)}$$

where v_i are the line-of-sight velocities of the GCs, and $\bar{v}$ and σ are allowed to vary as per the procedure below.

MCMC methods are quite sensitive to the priors assumed. Previous work (see e.g. Doppel et al. 2021; Toloba et al. 2023) favours the Jeffreys prior, which we implement. In theory, this assumption allows us to claim more ignorance (than, for example, a flat prior) on the location of the most likely parameters. For a Gaussian distribution, this amounts to multiplying the likelihood by a factor of $1/\sigma$, as the prior on $\bar{v}$ for this distribution is simply 1.

The MCMC calculation follows the Metropolis–Hastings technique to produce the posterior PDFs for σ and $\bar{v}$. In short, the method is as follows:

(i) for both σ and $\bar{v}$, initial guesses are made for their values
(ii) the likelihood is calculated assuming these values
(iii) randomly select one of the variables
(iv) from a Gaussian distribution centred on the randomly selected value with a dispersion on par with the expected errors, jump to a random value. We assume a dispersion of 5 km s^{-1} for this work.
(v) With this new value of the randomly selected parameter, calculate the likelihood again.

(a) If the new likelihood is greater than the old likelihood, then the new value of the randomly selected parameter is kept.
(b) If the new likelihood is less than the old likelihood, calculate the ratio of the new likelihood to the old. If this value is greater than a randomly selected number between 0 and 1, the new value of the parameter is accepted. Otherwise, it is rejected.

(vi) Repeat this algorithm until the parameter space of all parameters has been sufficiently explored. For this study, we repeat this process 10^5 times to ensure that the resultant posteriors are sufficiently converged.

The median and 25th–75th percentiles taken from the resultant posteriors constitute the values of σ_{MCMC} quoted in this work.

This paper has been typeset from a TEX/LATEX file prepared by the author.